Printability conditions for an all-solid-state laser transfer

Salvatore Surdo[1]*, Alberto Diaspro[1,2], and Martí Duocastella[1,3]*

[1]Nanoscopy, CHT Erzelli, Istituto Italiano di Tecnologia, Via Enrico Melen 83, Building B, 16152 Genova, Italy

[2]DIFILAB, Department of Physics, University of Genoa, Via Dodecaneso 33, 16146 Genova, Italy

[3]Departament de Física Aplicada, Universitat de Barcelona, C/Martí i Franquès 1, 08028 Barcelona, Spain

Corresponding author: salvatore.surdo@iit.it, marti.duocastella@iit.it

Abstract

Several laser technologies exist capable of adding solid materials to a targeted area of a substrate, including photopolymerization, laser sintering, or laser-induced forward transfer. However, the added material normally undergoes a phase change, causing adverse effects such as shrinkage, stress, or degradation. As recently demonstrated, this issue can be addressed by using laser pulses to mechanically delaminate and eject a disk from a film. In this case, the laser plays the role of a catapult, with minimal thermal damage to the transferred disk. Despite proven success in micro-electronics and micro-optics, little is known about the mechanical properties of the film that lead to a crack-free all-solid-state transfer. Here, we present a theoretical and experimental study on the effects that film rigidity, elasticity, and plasticity play on laser catapulting. By combining the thermodynamic equations of the laser-generated propulsion force with the theory of thin plate bending, we derived an analytical model that fully describes the list of events responsible for disk ejection. The model is in good agreement with experiments using elastomers, polymers, and metals. A complete printability map based on the film mechanical parameters is reported, which can help to broaden the family of materials suitable for laser additive manufacturing.

Keywords: additive manufacturing; LIFT; laser heating; plate bending; membrane stretching.

1. Introduction

Additive-manufacturing (AM) technologies offer remarkable opportunities for rapidly fabricating on-demand heterogeneous systems ranging from micro-optics to sensors [1–6]. Based on the direct deposition of a controlled amount of material on a targeted position of a substrate, they allow creating two-dimensional or three-dimensional solid structures with unprecedented precision. Successful examples include selective laser sintering [7,8], laser-induced forward transfer (LIFT) [9,10], fused deposition molding [11,12], or stereo-lithography [13,14]. While AM is shaping the future of scientific and industrial manufacturing, most existing techniques face a serious drawback – the transferred material typically undergoes a phase change, whether it is melting, vaporizing, or cross-linking. Such transition can cause degradation, shrinking, stress or oxidation, irreversibly compromising the properties of the added materials [15–17].

Efforts to address this issue include using lasers to delaminate and eject a disk from a film. Known in literature as laser decal transfer [18,19], laser catapulting [20,21] or simply a modified version of LIFT [22–24],

it enables the transfer of material in solid form with no phase change involved. As shown in Figure 1, under appropriate conditions a single laser pulse mechanically ruptures a film, named donor, supported by a laser-transparent substrate, named carrier. In this case, the first action of the laser pulse is to locally ablate a thin portion of the donor, forming a gas-pocket at the donor–carrier interface. Further interaction with the laser pulse heats up and expands the gas, causing a deflection of the delaminated donor until rupture occurs and a disk is ejected toward a nearby substrate. Excluding the upper part of the disk, which directly interacts with the laser, the transfer process occurs with negligible temperature changes.

To ensure successful delamination and transfer of a crack-free disk, two main conditions must be fulfilled. First, the laser must provide enough thrust, which requires a donor with strong optical absorption at the laser wavelength used. Proper selection of the laser source suffices to assure this condition. It can be further relaxed by adding an absorbing layer between donor and carrier, which will vaporize completely or partially when interacting with the laser pulse [25–27]. Secondly, the highest stresses during donor deflection must be localized at the edges of the delaminated region. This guarantees a clean rupture of the disk and prevents the typical volcanic-like craters induced by pulsed ablation. The central question is, for a given beam size, which mechanical properties of the donor, such as rigidity and elasticity, lead to high stresses at the edge of the disk. An answer is key to shed light on the constraints of laser catapulting and establish its niche applications, but it has not been provided yet.

Here we present an analytical model to describe the conditions that lead to suitable disk ejection in laser catapulting. Our model combines the thermodynamic equations for calculating the laser-induced pressure force with the classical theory of plate bending, namely the theory of mechanics that predicts how much bending a thin material or plate experiences under the action of an external force. As a result, printability maps can be obtained based on different laser parameters and the mechanical and geometrical characteristics of the donor. We validated our model by performing experiments with several solid donors, including elastomers, plastics, and metals. The study herein provides rules and conditions for an all-solid-state disk transfer, paving the way for exploiting laser catapulting as an AM tool for the design and implementation of delicate microsystems.

2. Model development

We divided our physical model into two distinct parts, namely laser-matter interaction and plate bending, as illustrated in Figure 2. First, we focused on establishing an analytical relation between laser energy and the resulting gas-pocket pressure. Such a pressure represents the thrust of the process, namely the mechanism responsible for deflecting a fraction of the donor. Secondly, we modeled, using the plate-bending theory, the deflection, and stresses of the donor generated for a given applied pressure. Two distinct cases can be distinguished

depending on the deflection expected. As detailed next, combining both parts provides a complete picture of laser catapulting and the conditions sufficient and necessary for successful, namely crack-free and congruent, transfer of all-solid-state disks.

2.1 Laser-induced pressure

The calculation of the pressure induced by the laser-generated gas-pocket poses a challenging problem. To simplify it, we assumed that the laser instantaneously vaporizes a thin portion of the donor. In other words, the laser-irradiated area was suddenly delaminated, generating a gas-pocket at the donor-carrier interface. For this to occur, the laser energy (E_L) must be higher than the donor latent heat of evaporation (H). If this condition were not fulfilled, the irradiated area would remain bonded to the carrier, impeding disk ejection.

We considered the size of the delaminated region to be determined by the beam waist with laser fluence exceeding the threshold for ablation, while the residual energy of the laser pulse was used to heat and expand the gas. The fraction of laser energy that was absorbed by the gas and converted into thermal energy is:

$$\Delta Q = K \int_0^{\tau_L} I(F,t)dt \qquad (1)$$

where I is the instantaneous laser power, F is the laser fluence (laser energy divided by the area of the laser spot), t denotes time, τ_L is the pulse duration, and K is the laser-to-thermal energy conversion efficiency that depends on the refractive index and optical absorption of the gas. In this study, we supposed I to have a temporal profile that corresponds to a Gaussian function, where its full-width at half-maximum equals the pulse duration, and its integral over the pulse duration is the laser energy.

Gas expansion is an adiabatic process, with pressure and volume changing accordingly. Given the complexity of modeling such a process analytically, we simplified it following a method previously described in the literature [28]. Briefly, we divided the laser pulse into infinitesimal time-steps ($\Delta t \ll \tau_L$). At the beginning of the i^{th} time-step (t_i), the adsorbed energy causes an isochoric increase in the temperature of the gas-pocket given by [28,29]:

$$\Delta T_i = \frac{\Delta Q_i}{m c_V} \qquad (2)$$

where m and ΔQ_i are mass and heat added to the gas at the i^{th} time-step. This rise in temperature leads to an increment of the gas pressure that can be calculated as:

$$\Delta P_i = n \frac{R}{V_{i-1}} \Delta T_i = \eta \frac{1}{V_{i-1}} \int_{t_i-\Delta t}^{t_i} I(F,\tau)\, d\tau \qquad (3)$$

where n is the amount of gas in moles, R is the universal gas constant, V_{i-1} is the volume of the gas at the end of the $(i\text{-}1)^{\text{th}}$ time-step, and $\eta = K \frac{nR}{m c_V}$ is the laser energy to the pressure-volume work conversion efficiency of the

system. This delta pressure is responsible for the deflection of the donor and thus for the isobaric expansion of the gas from V_{i-1} to V_i. In this model, the initial volume V_0 consists of a disk with an area equal to the beam size above the ablation threshold and a depth that is function of the laser penetration depth in the donor. For a given η, Eq.(3) is used to determine the initial pressure P_0.

When the time-step is ended, the pressure P_{i-1} is corrected to its adiabatic value, $P_i = P_{i-1}\left(\frac{V_{i-1}}{V_i}\right)^{\gamma}$, where γ depends on the gas specific heat at constant pressure and constant volume. Notably, in the limit of infinitesimal time-steps ($\Delta t \to 0$), this iterative process leads to a good model of the gas adiabatic expansion. However, both P_i and V_i depend on the film deflection (w_i) and the isobaric gas expansion ΔP_i. In other words, the laser induced-pressure depends on the mechanical properties of the donor. Therefore, the thermodynamic equations are intrinsically coupled with the bending of the donor. As shown below, we can use the thin plate theory to express w_i and V_i as functions of ΔP_i and, with this information, establish the conditions needed to eject a disk.

2.2 Bending under the action of the laser-induced pressure

To model the laser-induced deflection, we considered the delaminated region of the donor to be a thin plate clamped at its edges. The deflection of the plate due to the laser-induced gas pocket pressure is governed by the following partial differential equation [30]:

$$\nabla^2\nabla^2 w = -\frac{P_{i-1}+\Delta P_i}{D} \qquad (4)$$

where w is the vertical deflection, and D is the plate flexural rigidity defined as $D = \frac{Eh^3}{12(1-\nu^2)}$ with h, E and ν being film thickness, Young or elastic modulus, and Poisson ratio of the material. Notably, D quantifies the ability of the plate to resist deformations, namely stiffness or rigidity, and is key for material ejection.

2.2.1 The case of small deflections

A simplified solution of Eq.(4) can be found with the Kirchhoff-Love theory, suitable for the case of thin plates and small deflections (see Supplementary Information for a detailed list of the basic assumptions of this theory). Considering circular plates, cylindrical coordinates (r, θ, z), and an axial-symmetric load (the plate is not subject to twisting moments), Eq.(4) can be expressed as an ordinary differential equation in r, which has an exact analytical solution:

$$w_i(r) = -\frac{P_{i-1}+\Delta P_i}{64D} r^4 + A\ln(r) + B\ \frac{r^2}{2} + C\ \frac{r^2}{4}[2\ln(r) - 1] + D \qquad (5)$$

where, A, B, C, and D are constants to be determined by applying the appropriate boundary conditions. For a clamped circular plate, these are three: i) Small deflection at the center of the plate, $w_i(0) \ll h$; ii) The plate does not experience deflections at the edges, $w_i(r_p) = 0$; iii) The plate is flat at the edges, $\frac{dw_i}{dr}(r_p) = 0$. Such boundary conditions lead to a relationship between plate deflection and laser-induced pressure given by:

$$w_i(r) = -\frac{P_{i-1}+\Delta P_i}{64}(r_P^2 - r^2)^2 \ . \qquad (6)$$

From Eq.(6), the gas volume (V_i) at the end of the isobaric expansion can be obtained by integrating the plate deflection over the disk area:

$$V_i = \left|\int_0^{2\pi}\int_0^{r_P} w_i(r)\, r\, d\theta dr\right| = \frac{\pi}{192\, D}(P_{i-1} + \Delta P_i)\, r_P^6. \qquad (7)$$

Note that Eq.(7) constitutes the fundamental relationship needed to calculate the adiabatic laser-induced gas pressure. Indeed, combining Eq.(3) and (7) leads to:

$$P_i = \left(\frac{192}{\pi}\frac{D}{r_P^6}\right)^{\gamma} P_{i-1}\left(\frac{V_{i-1}}{P_{i-1} + \frac{\eta}{V_{i-1}}\int_{t_i-\Delta t}^{t_i} I(F,\tau)d\tau}\right)^{\gamma} \qquad (8)$$

The iterative solution of Eq.(8) enables evaluating the laser-induced pressure for a given laser pulse and material. With this information, the conditions for disk ejection can be derived, as described in section 3.1.

2.2.2 The case of large deflections

The solution reported in section 2.2.1 only applies to a limited range of materials and geometries. To generalize the solution and include the case of large deflections, which is likely to occur in laser catapulting of flexible materials, we can consider the set of nonlinear partial differential equations known as von Karman equations [30,31]. In general, an analytical solution of these equations is unattainable. Even if numerical approaches such as finite difference methods or finite element analysis exist, their high computational cost or issues with the convergence or stability of the solution can compromise their applicability. Alternatively, approximate solutions exist under certain assumptions. In the case of a thin and flexible circular plate subjected to an axisymmetric load, we can approximate plate deflection as [30,31]:

$$w(r) = w_{max}\left(1 - \frac{r^2}{r_P^2}\right)^2 \qquad (9)$$

where w_{max} is maximum deflection at the center ($r = 0$) of the plate, which for a clamped plate can be calculated by solving:

$$\frac{2}{21}\frac{23-9\,\nu}{1-\nu}\left(\frac{w_{max}}{h}\right)^3 + \frac{16}{3(1-\nu^2)}\left(\frac{w_{max}}{h}\right) = \frac{P_i}{E}\left(\frac{r_p}{h}\right)^4 \qquad (10)$$

Notably, Eq.(9) has the same functional form of the deflection we obtained for Kirchhoff-Love plates, with the difference that the maximum deflection is a nonlinear function of the laser-induced pressure P_i. Still, for $w_{max}/h \ll 1$, the first term on the right side of Eq.(10) is negligible, and the maximum deflection is linear with the applied load, as in the case of Kirchhoff plates. Eq.(9) and (10) can be used to calculate the laser-induced volume and pressure of the gas-pocket at the end of each time-step following the same procedure detailed for the small deflections, as shown in Fig. 3a-b.

3. Conditions for successful catapulting of disks

The previous sections provide an analytical model for the laser-induced pressure and plate deflection during laser catapulting. The open question is when such induced-pressure leads to the rupture of the donor and ejection of a crack-free disk. Considering thin plate theory, successful catapulting of disks occurs when two conditions are met: i) The highest pressure-induced stresses are located at the periphery of the plate; ii) The stresses at the periphery overcome the ultimate stress of the material. While the first one guarantees a clean rupture of the disk, the second one ensures that a disk is ejected. Therefore, deriving the analytical expressions of the laser-induced stresses is crucial to establish a printability map for the all-solid-state laser transfer.

3.1 The case of small deflections

The Kirchhoff-Love plate theory used in section 2.2.1 for small deflections only considers bending stresses. Using Eq. (7), they can be calculated as (see Supplementary information):

$$\sigma_r = -\frac{3z}{4h^3} r_p^2 (P_{i-1} + \Delta P_i) \left[(1+\nu) - \left(\frac{r}{r_p}\right)^2 (3+\nu) \right] \quad (11)$$

$$\sigma_\theta = -\frac{3z}{4h^3} r_p^2 (P_{i-1} + \Delta P_i) \left[(1+\nu) - \left(\frac{r}{r_p}\right)^2 (1+3\nu) \right] \quad (12)$$

Notably, the highest stresses are always radial and located at the edges ($r = r_p$) of the laser-delaminated region. Thus, condition (i) for ejection is always fulfilled, and disk transfer only depends on condition (ii) – disk transfer will occur when the laser-induced stress at the periphery of the plate $\sigma_{total}(r = r_p, z = \pm\frac{h}{2})$ overcomes the donor's ultimate tensile strength (UTS). In other words, the conditions for printing reduces to a single equation:

$$\sigma_{total}(r = r_p, z = \pm\tfrac{h}{2}) > \text{UTS} \quad (13)$$

The total stress can be calculated using the same iterative method described above, using an instant stress given by the equation:

$$\sigma_i = \pm\frac{3}{4}\left(\frac{r_P}{h}\right)^2 (P_{i-1} + \Delta P_i) \qquad (14)$$

where $\pm$ indicates that the lower surface of the plate is in compression, whereas the upper one is in traction. By combining Eq. (1), (2), (3) and (11), we can calculate σ_i as a function of the instantaneous laser energy:

$$\sigma_i = \frac{3}{4}\left(\frac{r_P}{h}\right)^2 \left(P_{i-1} + \eta\frac{1}{V_{i-1}}\int_{t_i-\Delta t}^{t_i} I(F,\tau)\,d\tau\ \right) \qquad (15)$$

The final value of σ_{total} can be obtained by integrating Eq. 14 over the course of the laser pulse duration.

3.2 The case of large deflections

For large deflections, not only bending stresses can play a significant role for disk ejection, but also additional stresses. In this case, the laser-induced pressure is transmitted partly by flexural rigidity (bending) and partly by membrane action (stretching) of the plate (Fig. 3c). The approximated solutions for the bending and stretching stresses, both radial and tangential, are given by the equations [31]:

$$\sigma^*_{rb} = \frac{w_{max}}{h}\frac{2}{1-\nu^2}\left[(1+\nu) - \left(\frac{r}{r_p}\right)^2 (3+\nu)\right] \qquad (16)$$

$$\sigma^*_{\theta b} = \frac{w_{max}}{h}\frac{2}{1-\nu^2}\left[(1+\nu) - \left(\frac{r}{r_p}\right)^2 (1+3\nu)\right] \qquad (17)$$

$$\sigma^*_{rs} = \frac{1}{6}\left(\frac{w_{max}}{h}\right)^2 \left[3 - 6\left(\frac{r}{r_p}\right)^2 + 4\left(\frac{r}{r_p}\right)^4 - \left(\frac{r}{r_p}\right)^6\right] \qquad (18)$$

$$\sigma^*_{\theta s} = \frac{1}{6}\left(\frac{w_{max}}{h}\right)^2 \left[3 - 18\left(\frac{r}{r_p}\right)^2 + 20\left(\frac{r}{r_p}\right)^4 - 7\left(\frac{r}{r_p}\right)^6\right] \qquad (19)$$

where the apex * denotes the dimensionless form of the stress respect to the reference $E \cdot h^2/r_p^2$, namely $\sigma^* = \sigma\left(r_p/h\right)^2/E$. For small deflections ($\frac{w_{max}}{h} \ll 1$), the contributions of Eq. (18-19) are negligible. Consequently, we recover the same situation described in section 3.1 – only bending stress acts on the laser-delaminated disk, with a maximum value located at the edge of the irradiated area. In this case, the first condition for ejection is automatically satisfied. Instead, for larger deflections, stretching can become significant, altering the overall stress distribution within the delaminated disk – the maximum stress value can potentially be located at the center, causing rupture of the laser-irradiated region.

To assess the printability conditions, it is convenient to simplify the parameter space regarding the stress effects. A valuable quantity is the equivalent von Mises stress, $\sigma_{vm} = \sqrt{\sigma_r^2 - \sigma_r\sigma_\theta + \sigma_\theta^2}$ with σ_r and σ_θ being the principal stresses in the radial and tangential directions (considering both the stretching and bending contributions). Using the von Mises stress, the conditions for an all-solid-state transfer can be written as:

$$\sigma^*_{vm}(r = r_p) > \sigma^*_{vm}(r = 0) \qquad (20)$$

$$\sigma_{vm} \geq UTS \qquad (21)$$

Figure 3d shows the calculated temporal evolution of the pressure and maximum von Mises stresses for the same parameters simulated in Fig. 3a-b and for UTS= 50 MPa. Under these conditions, the rupture of the donor occurs at t =60 ns ($\sigma_{vm} = UTS$). As proved by the calculated stress distribution on the deformed disk (insets of Fig. 3d), Eq. (20) and (21) are also satisfied. Therefore, a clean ejection of a solid disk is expected.

3.3 Printability map

The conditions for successful laser catapulting, summarized in Eq.(20-21) for the more general case of large deflection, involve a large number of variables including laser-induced pressure (P), elastic modulus (E) of the material, and geometries (h, r_p) of the delaminated donor. Using scale analysis, these parameters can be grouped into the dimensionless pressure $p = P\ \left(r_p/h\right)^4/E$, which greatly simplifies determining the conditions for an all-solid-state ejection (Fig. 4 and S1). In fact, the plot of ${\sigma^*}_b(r_p)/{\sigma^*}_b(0)$ versus p enables defining the threshold pressure below which condition (i) for successful disk transfer occurs, which is $p = 20$. This value enables rewriting this first condition for an all-solid-state transfer as:

$$P\ < 20\ E\ \left(\frac{h}{r_p}\right)^4 \qquad (22)$$

Similarly, we can write condition (ii) as (see Supplementary Information):

$$P > \frac{3}{4}\left[\left(\frac{1}{4}\left(\frac{r_p}{h}\right)^2 \frac{\sigma_{max}}{E}\right)^2 + 2\right]\left(\frac{h}{r_p}\right)^2 UTS \qquad (23)$$

From the previous two equations, it is possible to predict a printability map. As shown in Figure 5, we mapped the ultimate tensile strength and elastic modulus of various materials and calculated the minimal dimensionless pressure p_{min} for each σ and E couples on the map. The green areas of the map correspond to regions where ejection of solid disks with various aspect ratio, defined as $AR = h/2r_p$, can occur ($p_{min} < 20$). Two main features are evident from the map. First, the ejection is more likely to occur for stiff materials with high Young modulus. This can be credited to the ability of stiff materials to resist stretching that, in the framework of bending theory, implies that the delaminated donor behaves as a plate rather than as a membrane. Secondly, the range of material suitable for an all-solid-state transfer becomes larger for AR increasing from 0.001 to 0.1. This can be explained considering that, for a larger aspect ratio, the delaminated donor is more rigid and, as such, it favors the transmission of the laser-induced pressure to bending rather than stretching. Importantly, the printability map shows that, under appropriate conditions, it is possible to extend the use of an all-solid-state laser transfer to materials that have traditionally been unexplored, such as foams or plastics.

3.4 Experimental verification

To validate the proposed model, we irradiated donor films of materials with different mechanical properties, namely polydimethylsiloxane (PDMS), photoresist, and copper. The mechanical and geometrical characteristics of the donors and laser parameters of this experiment are reported in Table 1 [32–35]. In all cases, the laser beam has a top-hat profile. As predicted by the model, the transfer of PDMS at AR<0.1 failed and, importantly, the presence of flower-like craters in correspondence to the laser-irradiated regions proved the membrane behavior (stretching stress is significant) of the delaminated donor (Fig. 6a). The experiments with photoresist, a paradigmatic example of a polymeric donor, at AR~0.04 (Fig. 6b) and copper at AR~0.02 (Fig. 6c) further confirmed the validity of the proposed model. Indeed, the outcome of the laser-heating process in both cases was a regular array of polymeric and metallic disks at positions congruent with the irradiated laser beam. Note that only some deviations in the disk shape are visible. In the case of plastic disks, the base is larger than the beam waist. This can be attributed to the brittle fracture caused by the laser, which resulted in tilted cracks propagating through the donor thickness. Instead, metallic disks exhibit a slightly concave shape due to the ductile nature of copper and its transition from elastic to plastic deformations before fracturing. If we exclude second-order effects, such as fracture propagation or plastic deformation, our results clearly demonstrate that the proposed model is capable of predicting whether an all-solid-stat laser transfer of a disk with given mechanical properties and geometries occurs or not. As such the printability map provided here represents a valuable tool for selecting which solid-state donors are suitable for laser catapulting

4. Energetic considerations on laser catapulting

The sections above enable predicting which materials and aspect ratio are suitable for an all-solid-state laser transfer. In all cases, we assumed that the laser beam was energetic enough to induce ejection. The question remains in determining which laser fluence provides the laser-induced pressure necessary for ejection. Also, the energy conversion efficiency of the ejection process η, defined as the fraction of the laser energy (E_L), which is used to do the pressure-volume work ($V\Delta P$) that leads to ejection, is important to establish the potential thermal effects of the process. To clarify these points, we systematically studied the role that two of the most significant mechanical properties of the donor, namely flexural rigidity and elasticity, play on the fluence threshold and η.

Figure 7a shows representative images of disks transferred at the minimal laser fluence that lead to successful catapulting. Specifically, we used top-hat beams with different sizes (r_p) to catapult microdisks with radii from 10 to 60 μm from polymeric donors (E =8 GPa) with different thicknesses (h=2.5 and 10 μm) and,

hence, flexural rigidity D =10 and 750 GPa μm^3. To make the results statistically significant, several disks (up to 5) were catapulted for each radius. Note that, in all cases, the transferred disks exhibit a top surface that is perfectly congruent with the size of the laser spot, but their base is larger for the thicker donor. This is consistent with the ejection mechanism for an all-solid-state transfer that implies the generation of peripheral and tilted fractures and their propagation across the donor thickness. [20]. Interestingly, the fluence threshold decreases nonlinearly as r_p increases from 10 to 60 μm, while maintaining D constant (Fig. 7b). This behavior can be explained by considering the quadratic dependence of the bending stress on r_p/h, as described by our model in Eq. (15-17). Therefore, the laser-induced pressure and fluence necessary for ejection increase with the disk aspect ratio. From the values of threshold fluence, it is possible to calculate η using the model described above. As shown in Figure 7c, even if higher fluences are required for ejecting thicker disks, the laser energy is more efficiently used in this case. In fact, η for transferring 10-μm-thick disks is approximately one order of magnitude higher than for 2.5-μm-thick disks. This trend is consistent with the increase in rigidity as the donor becomes thicker, which makes thick disks less prone to stretching, and thus more energy can be devoted to bending and rupture. Also, η increases with the disk aspect ratio. Using a similar argument than before, low aspect ratio disks experience large deflections, and thus a large fraction of the laser energy is used to stretch the donor.

The effects of donor elasticity on threshold fluence and efficiency are summarized in Figure 7d-e. In this case, we printed disks from a photoresist, a brittle material, and copper, a ductile donor, with identical rigidity (D~10 GPa μm^3). As expected, in both cases the fluence threshold nonlinearly decreases with disk radii (Fig. 7d), confirming that low aspect ratio disks are less energetically demanding to transfer than high AR disks. Interestingly, the ejection of copper disks requires higher laser fluences than in the case of photoresist. Given that both materials, at the operation wavelength of our laser, exhibit similar absorption coefficients (10^5-10^6 cm^{-1}) and reflectivity (~2%) at the carrier-donor interface, we can explain such a difference considering their elastic properties. Indeed, ductile materials such as copper are expected to transfer less efficiency the laser energy into bending stresses – a significant fraction of the laser energy will be used for plastic deformation. Such a hypothesis is consistent with the plot shown in Figure 7e, in which the pressure-volume work done by the laser is about one order of magnitude larger for the ductile donor with respect to the brittle one.

Notably, all the results reported in this section are consistent with our model. Even if the plasticity of the donor is not explicitly considered, the model accurately predicts that low aspect ratio disks of brittle materials require the lowest laser fluence for transfer. In contrast, the highest efficiency of laser catapulting is obtained for high aspect ratio disks of brittle materials. Thus, these are the ideal conditions for printing delicate materials.

5. Conclusions

An analytical model coupling the thermodynamics of the laser-heated gas with the classical theory of plate bending provides a realistic description of laser catapulting. The all-solid-state transfer can be successfully explained as the result of a sequence of events, namely gas-pocket formation, donor deflection, and material ejection caused by the arrival of a single laser pulse at the carrier-donor interface. Disk transfer without phase change depends on several parameters, including strength and elastic modulus of the donor material, aspect ratio of the disk, and laser fluence. The proposed model sheds light on the pivotal role of the mechanical properties of the donor and the laser pulse energy necessary for an all-solid-state transfer, establishing a printability map that can be used by scientists of any discipline to predict the conditions for successful laser catapulting. The study reported herein can be extended to solid disks of arbitrary geometries by using numerical approaches (Fig. S2).

As our results demonstrate for the first time, the mechanical properties of the donor are key for the effective application of laser catapulting to a wide range of materials. The donor selection rules provided by our model can be used to extend the applications of laser additive manufacturing to a large number of novel and emerging applications that require sensitive materials, such as tissue-engineering, flexible, or organic electronics.

6. Materials and methods

6.1 Carrier, donor, and receiver preparation

Fused silica substrates (1 mm × 25 mm × 25 mm) were purchased from Solid Photon and used as carriers. For the experiments with elastomers, 100 nm of chromium was sputtered on top of the carrier and used as a dynamic release layer to promote donor delamination and expansion at the energies available in our laser workstation. The elastomeric donor was prepared by drop-casting a solution of PDMS (Sylgard184, Dow Corning) dissolved in heptane (10% volume fraction) on top of the carrier. After solvent evaporation, a PDMS film with a thickness of ~800 nm was obtained. The polymeric donors were attained by spin-coating a solution of photoresist (S-1813, Shipley) at 1500 rpm. Thickness control between 2.5 and 10 μm was achieved by properly adjusting the solvent concentration. The metallic donor was a 1-μm-thick copper sputter-coated on top of the carrier substrate. Thermal annealing at 350°C for 2 h was used to improve the crystalline quality of the material. The receiver substrate was a 1-mm-thick PDMS slice with a size of 10 mm ×10 mm. During laser catapulting, the donor was placed on top of the receiver substrate (in contact with it).

6.2 Implementation of laser catapulting

Laser-transfer experiments were performed using a 100 Hz KrF excimer laser (Coherent-CompexPro 110). The laser emits 20-ns pulses at the operation wavelength of 248 nm. The donor was irradiated using a mask-based projection system exploiting a 0.1 numerical aperture imaging lens. The laser pulse on the projection mask had an energy of 250 mJ and a rectangular beam profile with flat-top distribution on one axis (FWHM=30 mm) and a Gaussian distribution on the other axis (FWHM=12 mm). Control of the laser fluence was performed with a motorized and variable attenuator. The relative position of the laser beam and the substrate was controlled by a motorized XYZ stage. A CMOS camera integrated into the laser workstation was used for the real-time and direct inspection of the sample and to perform measurements of the laser spot size at the carrier-donor interface.

6.3 Morphological characterization

The morphology of laser irradiated elastomers, polymers, and metals was investigated using scanning electron microscopy (JSM-6390, JEOL) at an acceleration voltage of 10 kV. Before inspection, the sample surfaces were coated with 10 nm of gold in order to inhibit charge accumulation. Geometrical characterization of the disks was carried out with a bright-field optical microscope (DM2500 M, Leica).

6.4 Model implementation

The model of the all-solid-state laser-induced transfer was implemented in Matlab (Mathworks, license 40621185) following the flowchart of Fig. 2. The inputs of the algorithm included laser and material parameters. The former comprised wavelength (λ), pulse duration (τ_L), spot size (r_p), and fluence (F) of the laser. The material parameters were refractive index (n_D = 1.5817 and 1.3653 at λ=248 nm for photoresist and copper, respectively [36,37]), Young modulus (E), Poisson ratio (ν), and thickness (h) of the donor along with rethe fractive index of the carrier (n_{quartz} =1.5086 at λ=248 nm) and ratio of specific heats of the gas-pocket (γ). For γ, the gas resulting from laser-delamination of the material in this work was assumed bi-atomic (γ=7/5). The algorithm computes the initial volume V_0 of the gas-pocket, samples the laser pulse intensity at time steps (t_i) separated of $\Delta t = 0.01\ \tau_L$, and finally computes instantaneous pressure and volume of the gas-pocket, deflection, and stress of the delaminated donor. The computation also included the optical losses due to reflection of the laser at the air-carrier and carrier-donor interfaces that were calculated by using the Fresnel equations. The model can be extended to carriers with low optical transparency by including in the calculation the optical losses due to the absorption of the laser radiation during its propagation through the carrier. The conversion efficiency η was calculated by fitting the experimental fluence under the assumption that ejection occurs at the end of the pulse duration.

References

[1] J. Yoon, S.M. Lee, D. Kang, M.A. Meitl, C.A. Bower, J.A. Rogers, Heterogeneously Integrated Optoelectronic Devices Enabled by Micro-Transfer Printing, Adv. Opt. Mater. 3 (2015) 1313–1335. doi:10.1002/adom.201500365.

[2] A. Camposeo, L. Persano, M. Farsari, D. Pisignano, Additive Manufacturing: Applications and Directions in Photonics and Optoelectronics, Adv. Opt. Mater. 7 (2019). doi:10.1002/adom.201800419.

[3] A.D. Valentine, T.A. Busbee, J.W. Boley, J.R. Raney, A. Chortos, A. Kotikian, J.D. Berrigan, M.F. Durstock, J.A. Lewis, Hybrid 3D Printing of Soft Electronics, Adv. Mater. 29 (2017) 1–8. doi:10.1002/adma.201703817.

[4] Y. Huang, H. Wu, L. Xiao, Y. Duan, H. Zhu, J. Bian, D. Ye, Z. Yin, Assembly and Application of 3D Conformal Electronics on Curvilinear Surface, Mater. Horizons. 6 (2019) 642–683. doi:10.1039/C8MH01450G.

[5] C.W. Foster, H.M. Elbardisy, M.P. Down, E.M. Keefe, G.C. Smith, C.E. Banks, Additively Manufactured Graphitic Electrochemical Sensing Platforms, Chem. Eng. J. 381 (2019) 122343. doi:10.1016/j.cej.2019.122343.

[6] M. Makrygianni, A. Ainsebaa, M. Nagel, S. Sanaur, Y.S. Raptis, I. Zergioti, D. Tsamakis, Laser printed organic semiconductor PQT-12 for bottom-gate organicthin-film transistors: Fabrication and characterization, Appl. Surf. Sci. 390 (2016) 823–830. doi:10.1016/j.apsusc.2016.08.124.

[7] B. Nagarajan, Z. Hu, X. Song, W. Zhai, J. Wei, Development of Micro Selective Laser Melting: The State of the Art and Future Perspectives, Engineering. 5 (2019) 702–720. doi:10.1016/j.eng.2019.07.002.

[8] C.A. Chatham, T.E. Long, C.B. Williams, A review of the process physics and material screening methods for polymer powder bed fusion additive manufacturing, Prog. Polym. Sci. 93 (2019) 68–95. doi:10.1016/j.progpolymsci.2019.03.003.

[9] C.B. Arnold, P. Serra, A. Piqué, Laser Direct-Write Techniques for Printing of Complex Materials, MRS Bull. 32 (2007) 23–32.

[10] C.W. Visser, R. Pohl, C. Sun, G.W. Römer, B. Huis In 'T Veld, D. Lohse, Toward 3D Printing of Pure Metals by Laser-Induced Forward Transfer, Adv. Mater. 27 (2015) 4087–4092.

[11] Z. Liu, Y. Wang, B. Wu, C. Cui, Y. Guo, C. Yan, A critical review of fused deposition modeling 3D printing technology in manufacturing polylactic acid parts, Int. J. Adv. Manuf. Technol. 102 (2019) 2877–2889. doi:10.1007/s00170-019-03332-x.

[12] O.A. Mohamed, S.H. Masood, J.L. Bhowmik, Optimization of fused deposition modeling process parameters: a review of current research and future prospects, Adv. Manuf. 3 (2015) 42–53. doi:10.1007/s40436-014-0097-7.

[13] S. Waheed, J.M. Cabot, N.P. Macdonald, T. Lewis, R.M. Guijt, B. Paull, M.C. Breadmore, 3D printed microfluidic devices: Enablers and barriers, Lab Chip. 16 (2016) 1993–2013. doi:10.1039/c6lc00284f.

[14] L. Hirt, A. Reiser, R. Spolenak, T. Zambelli, Additive Manufacturing of Metal Structures at the Micrometer Scale, Adv. Mater. 29 (2017) 1604211. doi:10.1002/adma.201604211.

[15] X. Niu, S. Singh, A. Garg, H. Singh, B. Panda, X. Peng, Q. Zhang, Review of materials used in laser-aided additive manufacturing processes to produce metallic products, Front. Mech. Eng. 14 (2018) 282–298. doi:10.1007/s11465-019-0526-1.

[16] S.U. Zhang, Degradation classification of 3D printing thermoplastics using fourier transform infrared

spectroscopy and artificial neural networks, Appl. Sci. 8 (2018) 1224. doi:10.3390/app8081224.

[17] W. Ma, H. Su, J. Zhang, Q. Ren, H. Liu, E. Wang, J. Ren, Z. Lu, L. Liu, H. Fu, Effects of composition and solidification rate on growth striations in laser floating zone melted Al2O3/GdAlO3 eutectic ceramics, J. Am. Ceram. Soc. 101 (2018) 3337–3346. doi:10.1111/jace.15507.

[18] H. Kim, M. Duocastella, K.M. Charipar, R.C.Y. Auyeung, A. Piqué, Laser printing of conformal and multi-level 3D interconnects, Appl. Phys. A Mater. Sci. Process. 113 (2013) 5–8. doi:10.1007/s00339-013-7909-7.

[19] R.C.Y. Auyeung, H. Kim, A.J. Birnbaum, M. Zalalutdinov, S.A. Mathews, A. Piqué, Laser decal transfer of freestanding microcantilevers and microbridges, Appl. Phys. A Mater. Sci. Process. 97 (2009) 513–519. doi:10.1007/s00339-009-5433-6.

[20] S. Surdo, R. Carzino, A. Diaspro, M. Duocastella, Single-Shot Laser Additive Manufacturing of High Fill-Factor Microlens Arrays, Adv. Opt. Mater. 6 (2018) 1701190. doi:10.1002/adom.201701190.

[21] S. Surdo, A. Diaspro, M. Duocastella, Geometry-controllable micro-optics with laser catapulting, Opt. Mater. Express. 9 (2019) 2892. doi:10.1364/ome.9.002892.

[22] M. Feinaeugle, P. Gregorčič, D.J. Heath, B. Mills, R.W. Eason, Time-resolved imaging of flyer dynamics for femtosecond laser-induced backward transfer of solid polymer thin films, Appl. Surf. Sci. 396 (2017) 1231–1238.

[23] P. Delaporte, A.-P. Alloncle, Laser-induced forward transfer: A high resolution additive manufacturing technology, Opt. Laser Technol. 78 (2016) 33–41. doi:10.1016/j.optlastec.2015.09.022.

[24] R. Fardel, M. Nagel, F. Nüesch, T. Lippert, A. Wokaun, Laser-Induced Forward Transfer of Organic LED Building Blocks Studied by Timed-Resolved Shadowgraphy, J. Phys. Chem. C. (2010) 5617–5636. doi:10.1021/jp907387q.

[25] N.T. Kattamis, P.E. Purnick, R. Weiss, C.B. Arnold, Thick film laser induced forward transfer for deposition of thermally and mechanically sensitive materials, Appl. Phys. Lett. 91 (2007). doi:10.1063/1.2799877.

[26] M. Duocastella, a. Patrascioiu, V. Dinca, J.M. Fernández-Pradas, J.L. Morenza, P. Serra, Study of liquid deposition during laser printing of liquids, Appl. Surf. Sci. 257 (2011) 5255–5258. doi:10.1016/j.apsusc.2010.10.148.

[27] C. Boutopoulos, I. Kalpyris, E. Serpetzoglou, I. Zergioti, Laser-induced forward transfer of silver nanoparticle ink: Time-resolved imaging of the jetting dynamics and correlation with the printing quality, Microfluid. Nanofluidics. 16 (2014) 493–500. doi:10.1007/s10404-013-1248-z.

[28] N.T. Kattamis, M.S. Brown, C.B. Arnold, Finite element analysis of blister formation in laser-induced forward transfer, J. Mater. Res. 26 (2011) 2438–2449. doi:10.1557/jmr.2011.215.

[29] M. Castillejo, P.M. Ossi, L. Zhigilei, Lasers in Materials Science, Springer International Publishing, Cham, 2014. doi:10.1007/978-3-319-02898-9.

[30] S. Timoshenko, S. Woinowsky-Krieger, Theory of plates and shells, McGraw-Hill, New York, 1959.

[31] E. Ventsel, T. Krauthammer, Thin Plates and Shells: Theory, Analysis, and Applications, 1st ed., Marcel Dekker INc., New Yoor, 2001.

[32] I.D. Johnston, D.K. McCluskey, C.K.L. Tan, M.C. Tracey, Mechanical characterization of bulk Sylgard 184 for microfluidics and microengineering, J. Micromechanics Microengineering. 24 (2014). doi:10.1088/0960-1317/24/3/035017.

[33] A. Müller, M.C. Wapler, U. Wallrabe, A quick and accurate method to determine the Poisson's ratio and the coefficient of thermal expansion of PDMS, Soft Matter. 15 (2019) 779–784. doi:10.1039/c8sm02105h.

[34] L. Calabri, N. Pugno, A. Rota, D. Marchetto, S. Valeri, Nanoindentation shape effect: Experiments, simulations and modelling, J. Phys. Condens. Matter. 19 (2007) 1–12. doi:10.1088/0953-8984/19/39/395002.

[35] B. Ross, Materials Specification Handbook, 4th ed., Ross Materials Technology Ltd, Glasgow, 1992. doi:10.1007/978-1-4615-3482-2.

[36] MicroChem Resist, (n.d.). http://www.microchem.com/pdf/PMMA_Data_Sheet.pdf (accessed September 19, 2019).

[37] P.B. Johnson, R.W. Christy, Optical constants of the noble metals, Phys. Rev. B. 6 (1972) 4370–4379. doi:10.1103/PhysRevB.6.4370.

Tables

Material	Elastic modulus[a] (GPa)	Poisson ratio[a] (–)	Ultimate strength[a] (MPa)	Thickness[b] (µm)	Flexural Rigidity[c] (GPa µm^3)	Aspect Ratio[b] (-)
PDMS	0.002	0.5	3.51–7.65	0.8	n.r.	0.013
Photoresist	8	0.33	50	2.5	10	0.04
				10	750	0.16
Copper	117	0.33	200-220	1	10	0.02

Table 1. Mechanical and geometrical parameters of the donors used in current experiments. [a] Published data, [b] Measured data, [c] Calculated data.

Figure and captions

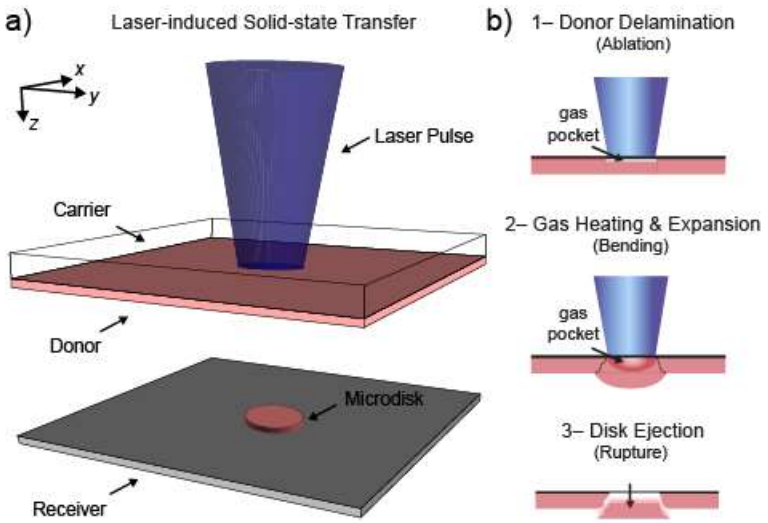

Fig. 1. All-solid-state laser transfer. a) Schematic of the experimental configuration used in laser-induced forward transfer. b) Cartoon depicting the sequence of events for the solid-state transfer: 1) Donor delamination and gas-pocket formation; 2) Donor deflection due to the laser-heating and expansion of the gas; 3) Mechanical rupture and ejection of a solid state disk.

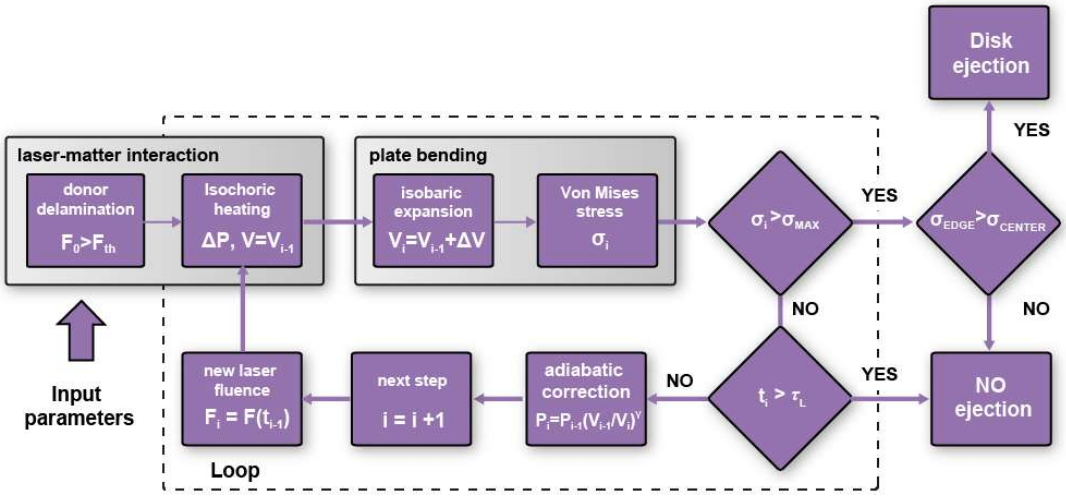

Fig. 2. Flowchart of the decision algorithm for ejection of a solid disk. The algorithm receives as inputs the laser parameters (wavelength, pulse duration, spot size, energy) as well as optical (refractive index), mechanical (Young modulus, Poisson ratio, ultimate strength), and geometrical (thickness) properties of the donor. The dashed line corresponds to the iterative loop used for establishing whether disk ejection occurs during the laser pulse.

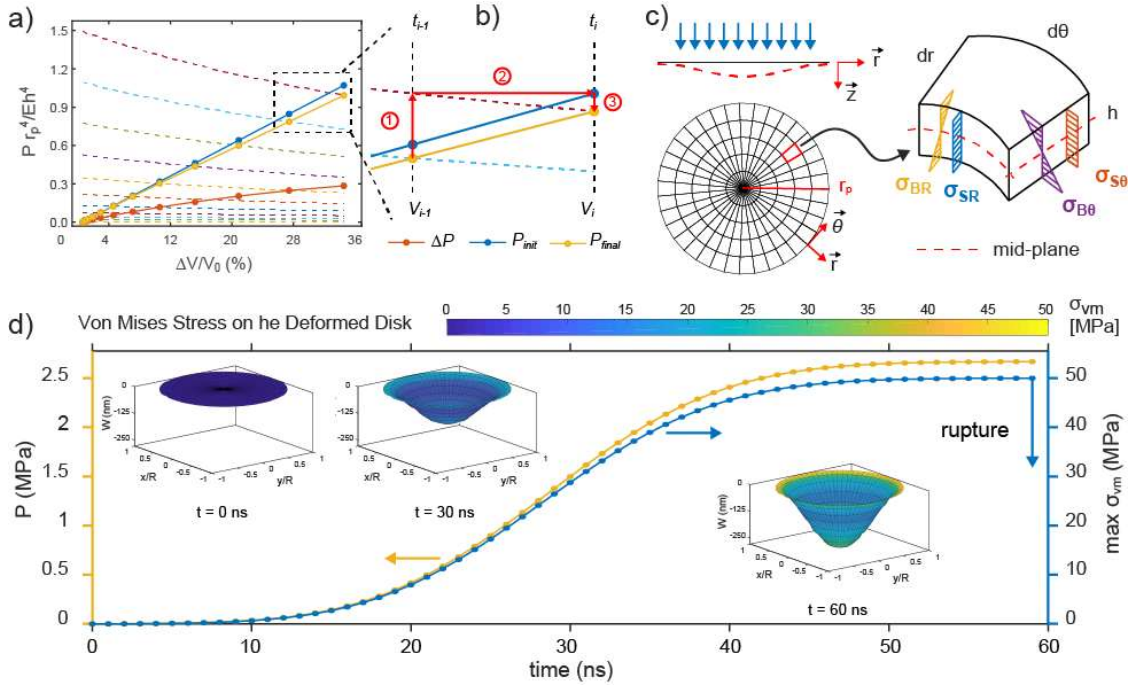

Fig. 3. All-solid-state transfer for large deflections. a) PV diagram of the laser-induced pressure, namely isochoric heating (red lines and symbols), isobaric expansion (blue lines and symbols), and adiabatic correction (yellow lines and symbols). The dashed lines denote a family of adiabatic curves. Parameters considered: τ_L =20 ns, r_p = 10 μm, F=120 mJ cm^{-2}, E =8 GPa, υ =0.33, and h =2 μm. b) Details of the strategy used to model the laser-expansion. c) Schematic description of the stress on the deformed donor under the action of a uniform laser-induced load. Radial (blue) and tangential (red) stretching stresses as well as radial (yellow) and tangential (violet) bending stresses act on each volume element. d) Calculated laser-induced pressure (yellow line and symbols) and stress (blue line and symbols) as a function of the laser pulse duration. The insets show the stress distribution on the deformed disk for various time steps within the laser pulse duration.

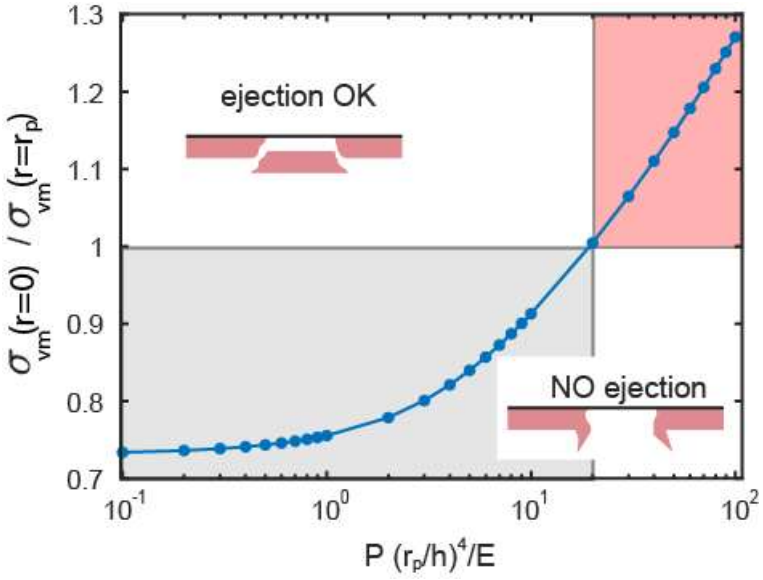

Fig. 4. Necessary condition for disk ejection. Ratio of the stress at the center to the stress at the edge as a function of the dimensionless induced pressure $p = P\left(r_p/h\right)^4/E$. Ejeciotn of the delaminated donor occurs for $P\left(r_p/h\right)^4/E \lesssim 20$ (gray area), while for larger pressures (red area) the donor exhibits a membrane behavior.

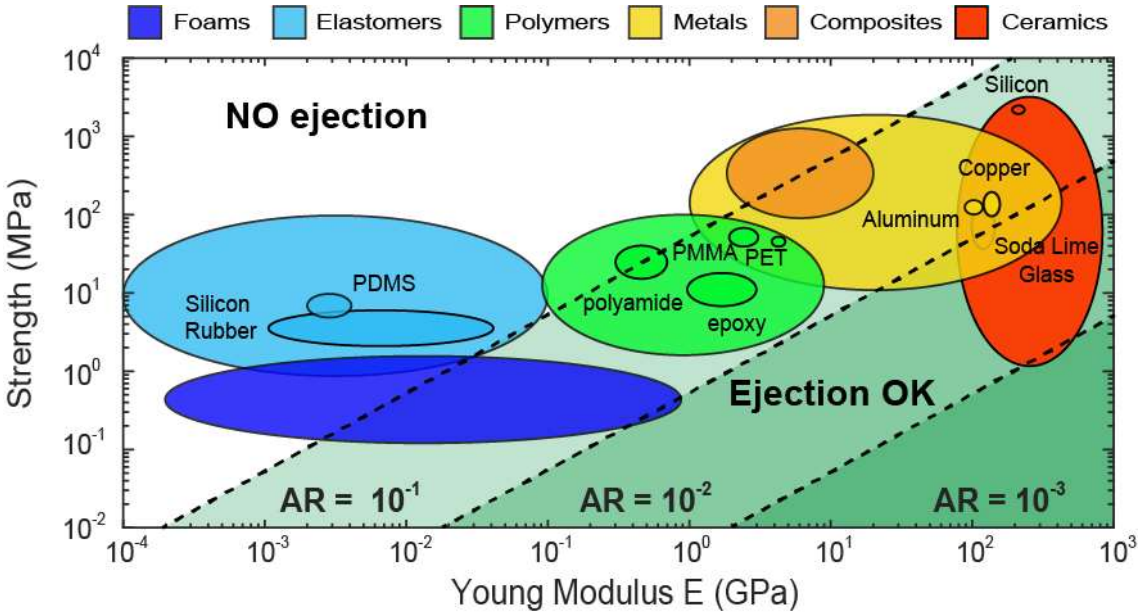

Fig. 5. Printability map. a) Ultimate strength-elastic modulus chart of material with various mechanical properties such as rigidity or elasticity. The green areas correspond to σ, E, and AR values that stratify the conditions for proper material ejection. Increasing the AR of the target disk from 0.001 to 0.1 clearly expands the donor options of an all-solid-state laser transfer.

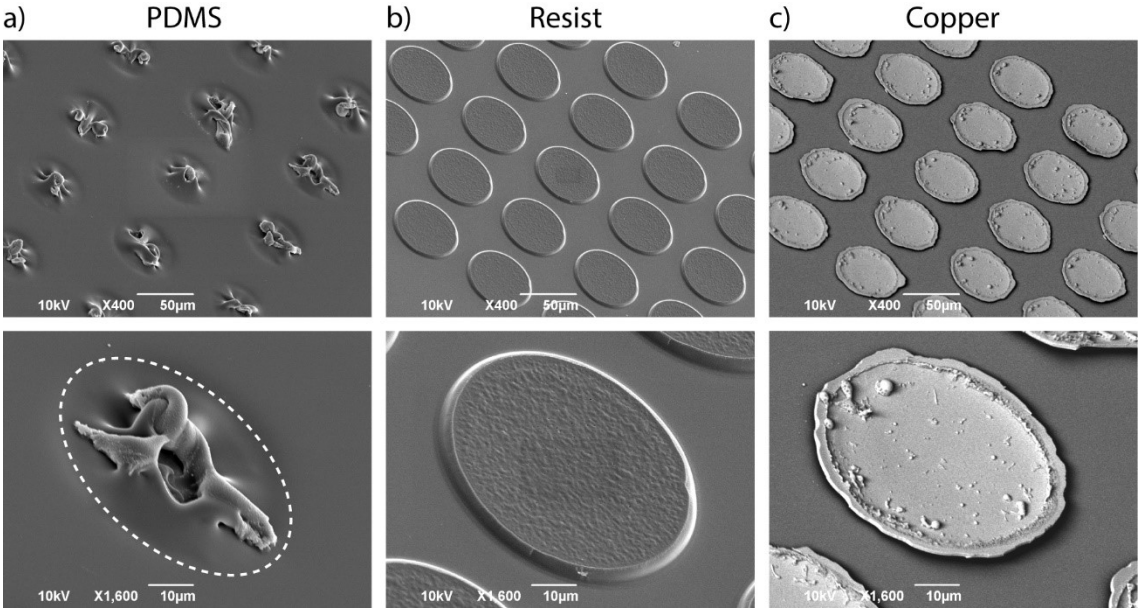

Fig. 6. Scanning electron micrographs illustrating the outcomes of laser catapulting of materials with different mechanical properties. a) Prospective view of an elastomeric donor after the irradiation with laser pulses at fluence of 350 mJ cm^2. The presence of craters highlights the membrane behavior of the donor. b-c) Prospective view of polymeric (b) and metallic (c) disks laser-printed at fluence of 75 and 250 mJ cm^2, respectively. The magnified SEM images (second row) highlight the different behavior between elastic (PDMS), brittle (resist), and ductile (copper) donors. The thicknesses of the donors used in this experiment are 0.8 (PDMS), 2 (resist), and 1 µm (copper).

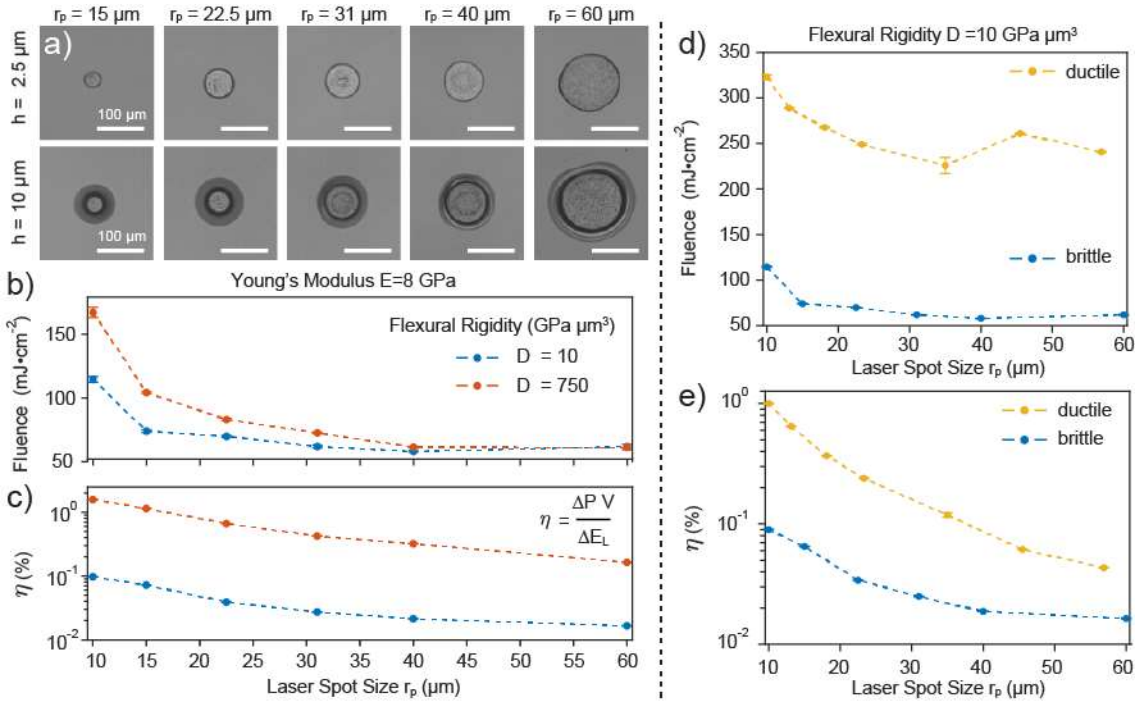

Fig. 7. Energy study of laser catapulting. a) Optical images of some representative polymeric (resist) disks with thicknesses of 2.5 µm (top row) and 10 µm (bottom row) and various radii (15, 22.5, 31, 40, and 60 µm). b) Fluence thresholds, mean values (symbols) and standard deviations (bars), for proper material ejection as a function of the flexural rigidity *D* and radius of the delaminated donor. c) Efficiency in the conversion of the laser energy into mechanical work at the threshold for material transfer. d-e) Fluence threshold and energy conversion efficiency, mean values (symbols) and standard deviations (bars), for delaminated donors with identical rigidity D~10 GP µm^3, radius in the same interval, and Young modulus of 8 GPa (resist) and 117 GPa (copper). Dashed lines are added in (b-e) to guide the eye.